Influence of irradiation on the space-time structure of shock waves

J. A. Maruhn,[1] I. N. Mishustin,[1,2,3] and L. M. Satarov[1,2]
[1]*Institut für Theoretische Physik, J.W. Goethe Universität, D-60054 Frankfurt am Main, Germany*
[2]*The Kurchatov Institute, Russian Research Center, 123182 Moscow, Russia*
[3]*The Niels Bohr Institute, DK-2100 Copenhagen Ø, Denmark*
(Received 2 August 2001; published 26 November 2001)

The long-range energy deposition by heavy-ion beams makes new shock wave experiments possible in the laboratory. We have investigated a situation that is of relevance to supernova dynamics in astrophysics, where a shock wave is irradiated by a flux of neutrinos depositing energy throughout the shock wave and surrounding matter, thus changing the behavior of the running shock. We have carried out fluid-dynamical simulations to study generic features of stimulated shock waves. First we consider an idealized case assuming uniform energy deposition into a planar shock wave propagating through an ideal gas. Then we investigate more realistic situations realizable in laboratory experiments with heavy-ion beams. We have found that energy deposition leads to two important effects: acceleration of the shock front and decay of the shock strength. The possibility of laboratory experiments is briefly discussed.

DOI: 10.1103/PhysRevE.64.066305 PACS number(s): 47.40.Nm, 47.70.Nd, 62.50.+p, 79.20.Rf

I. INTRODUCTION

Supernova explosions represent one of the most spectacular phenomena in our Universe. In recent years much effort has been devoted to developing realistic theoretical models of this complex process (see the recent review [1]). The main mechanism includes the shock wave generation upon the bounce of the infalling iron core of a massive star, but detailed calculations showed that the prompt bounce shock mechanism does not lead directly to ejection of the stellar envelope. Due to severe energy losses due to, e.g., photodisintegration of iron nuclei, the outward shock wave stops inside the iron core. Recently several new mechanisms of the shock revival have been suggested [2,3] that include neutrino heating and convection in the postshock matter. These processes raise the postshock pressure and provide additional energy for the shock wave expansion. The calculations performed by various groups differ, however, in conclusions concerning the possibility of successful shocks. In this rather unclear situation a better understanding of the stimulated shock dynamics is highly desirable [3]. Fortunately, intense heavy-ion beams open a new possibility to study such processes in laboratory experiments.

In the first part of this paper we formulate a simple model to study the evolution of a planar shock wave under influence of homogeneous irradiation. We have performed detailed fluid-dynamical calculations for the ideal gas equation of state. The matter flow behind the shock front is rather complicated, resembling a decay of an initial discontinuity [4]. The calculations show that under irradiation the shock front accelerates, but the density jump at this front diminishes. It is remarkable that a self-similar regime of hydrodynamic flow is established at large irradiation time.

In the second part of the paper we generalize our model to consider more realistic situations that may be easily reproduced in laboratory conditions. Namely, we consider the case when the initial shock wave is created by a beam with finite extension in the transverse directions. Specifically, we study the scenario in which the first beam creates a shock wave in a cylindrical target and then, when it has developed sufficiently, the target is irradiated by a second beam. The target length is chosen in such a way that the shock generated at the initial stage is completely within the deposition region of the second beam [5]. In our simulations we assume that both are heavy-ion beams with equal properties and are directed along the target axis from opposite directions. General properties of hydrodynamical flow in such targets have been studied earlier in Ref. [6]. Another interesting phenomenon is predicted for the case of a single beam irradiation with constant temporal profile. It is shown that with increasing irradiation time, when radial flow of matter behind the shock front becomes noticeable, the shock wave in its central parts decays as compared to initial stages. The origin of this phenomenon consists in the increased range of the bombarding particles at later stages of target irradiation.

The paper is organized as follows. In Sec. II a simple fluid-dynamical model is formulated for the case of homogeneous energy deposition. Then in Sec. III this model is used to study the dynamics of a planar shock wave in matter with an ideal gas equation of state. The asymptotic regime of the matter flow is considered by a semi-analytic method outlined in the Appendix. The results of more realistic calculations and suggestions for future experiments with heavy-ion beams are given in Sec. IV. The main results of the present paper are summarized in Sec. V.

II. EQUATIONS OF FLUID DYNAMICS

Let us consider a beam of energetic particles irradiating a target with the mass density ρ. Often we shall speak about photon irradiation, but the same approach can be applied for other penetrating particles, e.g., for neutrino beams. The strength of irradiation is characterized by the energy deposited per unit space-time volume in the local rest frame of the target,

$$\frac{dE}{dt\,d^3r} = \lambda\rho, \tag{1}$$

where λ is the specific deposition rate. Let the target consist of atoms of different species i with particle number densities n_i. In the case of monochromatic photons with the energy flux $I(\omega)$ one has

$$\lambda\rho = I(\omega)\sum_i n_i\langle\sigma_i^{\rm abs}(\omega)\rangle, \tag{2}$$

where $\hbar\omega$ is the photon energy, $\langle\sigma_i^{\rm abs}\rangle$ is the cross section of photon absorption on atoms of the ith kind. The angular brackets denote averaging over their momentum distribution. In this paper we neglect internal heat transport processes and assume λ to be constant in time and space. The last assumption implies that the external radiation is homogeneous, Doppler effects are not important, and the photon absorption length, $(\Sigma_i n_i\langle\sigma_i^{\rm abs}\rangle)^{-1}$, is large as compared to the characteristic size of a target.

Below it is assumed that energy deposition proceeds under condition of local thermodynamic equilibrium, in particular, we neglect effects of internal heat transport and viscosity. The dynamics of target flow is described by the equations of ideal hydrodynamics in nonrelativistic approximation. Let us consider first a one-dimensional case when matter moves along the x axis with the velocity $v\equiv v_x$. The equations of motion then take the form

$$\partial_t\rho + \partial_x(\rho v) = 0, \tag{3}$$

$$\partial_t(\rho v) + \partial_x(P+\rho v^2) = 0, \tag{4}$$

$$\partial_t(\epsilon+\rho v^2/2) + \partial_x[v(\epsilon+P+\rho v^2/2)] = \lambda\rho. \tag{5}$$

Here P is pressure and ϵ is the energy density. By using Eqs. (3) and (4) and thermodynamic relations one may rewrite Eq. (5) in the equivalent form

$$T(\partial_t + v\partial_x)s_m = \lambda, \tag{6}$$

where T is temperature and s_m is the specific entropy. This equation shows that λ is, in fact, the specific rate of heat deposition into the target matter.

In the following we assume that the target matter can be regarded as an ideal Boltzmann gas with one species of molecules and a constant ratio of heat capacities $\gamma = C_p/C_{\rm v}$. The equation of state of such matter has a very simple form

$$P = (\gamma-1)\epsilon = \rho RT/M, \tag{7}$$

where R is the gas constant and M is the molar mass. The specific entropy in this case is

$$s_m = \frac{R}{(\gamma-1)M}\ln\frac{P}{\rho^\gamma} + \text{const}. \tag{8}$$

Using Eq. (7) and introducing the specific volume $V = 1/\rho$ one can rewrite Eqs. (3)–(5) as follows

$$(\partial_t + v\partial_x)V = V\partial_x v, \tag{9}$$

$$(\partial_t + v\partial_x)v = -V\partial_x P, \tag{10}$$

$$V(\partial_t + v\partial_x)P + \gamma P(\partial_t + v\partial_x)V = (\gamma-1)\lambda. \tag{11}$$

It is convenient to introduce instead of P,V,v new dimensionless quantities $\overline{P} = P/P_0$, $\overline{V} = \rho_0 V$, $\overline{v} = v/v_0$ where P_0 and ρ_0 are initial pressure and density, and

$$v_0 = \sqrt{P_0/\rho_0}. \tag{12}$$

Let us make the transition from t,x to dimensionless variables $\overline{t} = t/t_0$ and $\overline{x} = x/x_0$, where

$$t_0 = v_0^2/\lambda, \quad x_0 = v_0 t_0. \tag{13}$$

Now Eqs. (9)–(11) may be rewritten in the same form, but with the replacements $P,V,v,t,x \to \overline{P},\overline{V},\overline{v},\overline{t},\overline{x}$ and $\lambda \to 1$. If the initial conditions do not impose additional scales, there is no need to solve fluid-dynamical equations for different deposition rates λ. It is sufficient to find the solution only for one fixed value of λ, then the above scaling can be used to obtain the solution for other values. For example, this scaling can be applied for the shock wave initial conditions (see the next section).

We close the general discussion by defining three families of characteristics $x_{C_+}, x_{C_-}, x_{C_0}$. They are solutions of the following differential equations

$$\dot{x}(t) = v + c_s \quad (C_+), \tag{14}$$

$$\dot{x}(t) = v - c_s \quad (C_-), \tag{15}$$

$$\dot{x}(t) = v \quad (C_0), \tag{16}$$

where v and c_s are taken at $x = x(t)$. As well known [4], these characteristics describe propagation of small disturbances of fluid-dynamical quantities. In particular, the entropy disturbances propagate along the C_0 characteristics (the latter are also the collective flow trajectories).

In the following we assume that irradiation starts at $t=0$ and the initial profiles $\rho(x,0)$, $v(x,0)$ and $P(x,0)$ are known function of x. Let us consider first the case of homogeneous initial conditions, when $\rho(x,0)=\rho_0$, $v(x,0)=\mathrm{v}_0$, and $P(x,0)=P_0$. In this case the solution of Eqs. (9)–(11) is trivial

$$V(x,t) = 1/\rho_0, \tag{17}$$

$$v(x,t) = \mathrm{v}_0, \tag{18}$$

$$P(x,t) = P_0 + (\gamma-1)\rho_0\lambda t. \tag{19}$$

In the same case the adiabatic sound velocity is equal to

$$c_s = \sqrt{\gamma PV} = \sqrt{c_0^2 + \gamma(\gamma-1)\lambda t}, \tag{20}$$

where $c_0 = \sqrt{\gamma P_0/\rho_0}$ is the initial sound velocity.

For homogeneous initial conditions, substituting Eqs. (18) and (20) into Eqs. (14)–(16), one can find characteristics analytically

$$x_{C_\pm}(t)=\mathrm{v}_0 t\pm\frac{2}{3\gamma(\gamma-1)\lambda}[c_0^2+\gamma(\gamma-1)\lambda t]^{3/2}+\text{const}, \tag{21}$$

$$x_{C_0}(t)=\mathrm{v}_0 t+\text{const}. \tag{22}$$

According to Eq. (21), at large irradiation times the $C_\pm$ characteristics approach asymptotically the same lines that do not depend on initial conditions

$$x_{C_\pm}(t)\simeq\pm\xi_0\sqrt{\lambda t^3}\quad(t\gg c_0^2/\lambda,\mathrm{v}_0^2/\lambda), \tag{23}$$

where

$$\xi_0=\frac{2}{3}\sqrt{\gamma(\gamma-1)}. \tag{24}$$

III. ONE-DIMENSIONAL SHOCK WAVES

A. Numerical results

Let us consider a one-dimensional shock wave propagating to the left along the x axis (directed to the right) and denote the position of its front by $x_{\mathrm{sh}}(t)$. For brevity we introduce the vector $\boldsymbol{y}=(V,v,P)$ that combines the set of fluid-dynamic quantities in a compact way. It is assumed that at $x=x_{\mathrm{sh}}$ this vector jumps from $\boldsymbol{y}_1\equiv\boldsymbol{y}(x_{\mathrm{sh}}-0,t)$ to $\boldsymbol{y}_2\equiv\boldsymbol{y}(x_{\mathrm{sh}}+0,t)$. In the rest frame of the shock wave (moving with the velocity $D=|\dot{x}_{\mathrm{sh}}|$ with respect to the laboratory frame) the fluxes of mass, energy, and momentum should be continuous at $x=x_{\mathrm{sh}}$. This gives three relations [4] connecting D and the components of vectors $\boldsymbol{y}_{1,2}$. In the case of an ideal gas one obtains [7]

$$\frac{v_1+D}{V_1}=\frac{v_2+D}{V_2}=\sqrt{\frac{P_2-P_1}{V_1-V_2}}=\sqrt{\frac{\gamma(P_1+P_2)}{V_1+V_2}}, \tag{25}$$

where $v_{1,2}$ are defined in the laboratory frame. Therefore, at given $\boldsymbol{y}_1$, all characteristics of the shock wave can be determined if one of the quantities D,P_2,V_2,v_2 is known. One should bear in mind that the relations (25) are based only on the local conservation laws and hold also for shock waves with energy deposition. However, as will be shown below, in this situation the characteristics of the shock wave (in particular, D) are in general time dependent.

It is further assumed that a steplike one-dimensional shock wave was created in a target at $t<0$. If pressure and density before and behind the shock front do not change with x and t, the shock velocity D will be constant. Below we study the dynamics of this ''initial'' shock wave after switching on the energy deposition at $t=0$. Equations (9)–(11) are solved numerically by using the flux corrected transport (FCT) algorithm [8]. The calculations are performed in the rest frame of the initial shock. Choosing the origin of the x axis at the position of the shock front, one has $x_{\mathrm{sh}}(t)=0$ at $t<0$. To be more specific, the following initial conditions are applied

$$\boldsymbol{y}(x,0)=\boldsymbol{y}_{10}\Theta(-x)+\boldsymbol{y}_{20}\Theta(x), \tag{26}$$

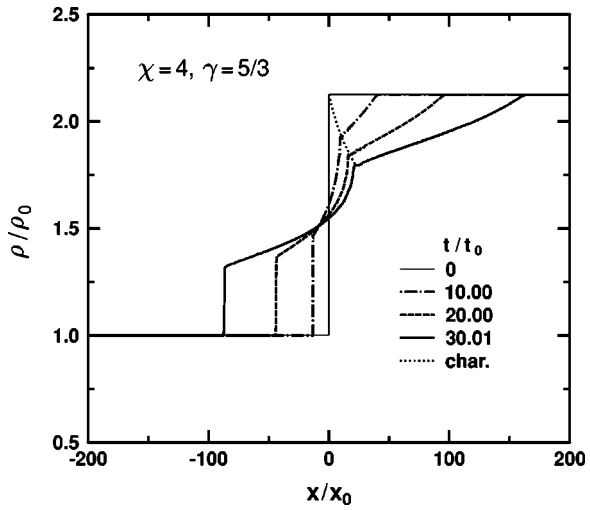

FIG. 1. Density profiles for different times of shock wave irradiation. The initial pressure ratio $\chi=4$. Scales x_0 and t_0 are given by Eqs. (12) and (13). The dotted curve shows densities on the C_0 characteristic with $x(0)=0$.

where $\Theta(x)\equiv\frac{1}{2}(1+\mathrm{sgn}\,x)$, and $\boldsymbol{y}_{10}$ and $\boldsymbol{y}_{20}$ denote the fluid-dynamical quantities in front and behind of the initial shock front, respectively. We choose these quantities by fixing the density ($\rho_0\equiv\rho_{10}=1/V_{10}$) and pressure ($P_0\equiv P_{10}$) at $x<0$ as well as the pressure (P_{20}) at $x>0$.

Using the relations (25) one has

$$V_{20}=\frac{(\gamma-1)\chi+\gamma+1}{(\gamma+1)\chi+\gamma-1}V_{10}, \tag{27}$$

$$v_{10}=v_{20}\frac{V_{10}}{V_{20}}=D(0)=v_0\sqrt{\frac{(\gamma+1)\chi+\gamma-1}{2}}, \tag{28}$$

where $\chi=P_{20}/P_{10}$ is the initial pressure ratio, v_0 is defined by Eq. (12), and the velocities v_{i0} ($i=1,2$) are taken in the rest frame of the shock front.

Most calculations have been performed for $\gamma=5/3$ and $\chi=4$. In this case the initial density jumps at the shock front from ρ_0 to $2.125\,\rho_0$ and the flow velocity jumps from $v_{10}\simeq 2.380\,v_0$ to $v_{20}\simeq 1.120\,v_0$. Some results of numerical calculations for these initial conditions are shown in Figs. 1–4. The results are presented using the scaled variables t/t_0 and x/x_0, with t_0,x_0 defined in Eq. (13). As explained in the preceding section, in such a representation the whole λ dependence is contained only in the scales t_0 and x_0.

Figure 1 shows the density profiles at different times from the beginning of irradiation. One can see that irradiation deforms the shape of the initial shock wave at $t>0$. The region of the perturbed flow is wider at later times. With increasing t the shock wave becomes weaker (the density jump at the left hand side diminishes). However, the absolute value of the shock front velocity becomes larger as compared to the initial value $D(0)$.

The acceleration of the shock front is clearly visible in Fig. 1. Indeed, the shift of the shock front position from the point $x=0$ increases nonlinearly with t. The reason for ac-

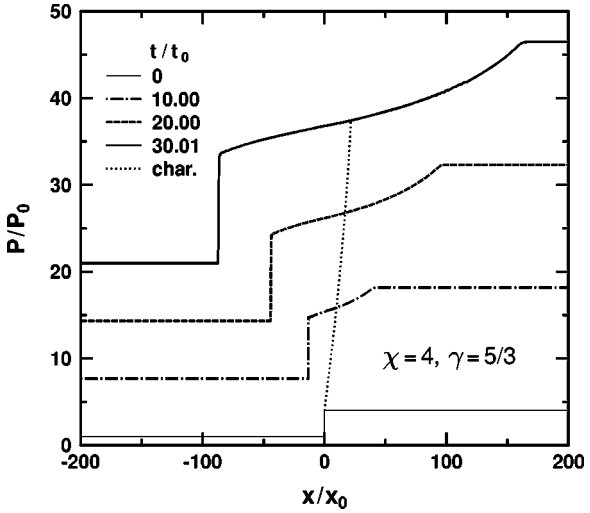

FIG. 2. The same as in Fig. 1, but for pressure profiles.

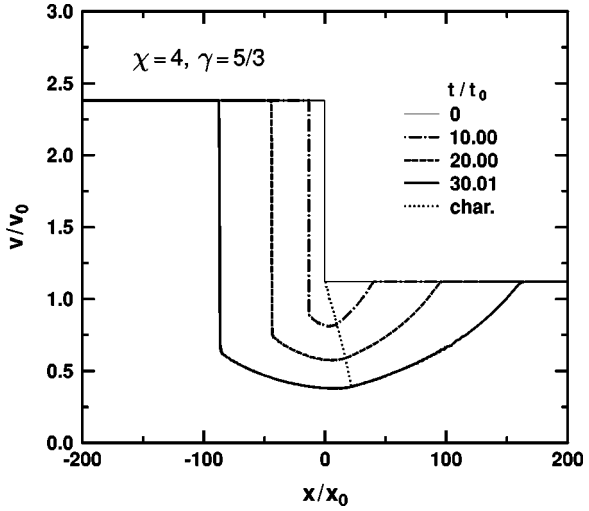

FIG. 4. The same as in Fig. 1, but for flow velocity profiles.

celeration is rather simple: as follows from Eq. (20) and Fig. 3 the sound velocity c_s behind the shock front increases with t due to the heat deposition.

At given t the density profile has three characteristic points: (1) the shock wave discontinuity at $x=x_{\rm sh}(t)$, (2) the intermediate kink where the derivative $\partial_x\rho$ jumps, and (3) the boundary of the perturbed region on the right-hand side. The position of the third point can be found analytically. It is in fact the characteristic $x_{C_+}(t)$ with the initial condition $x_{C_+}(0)=0$. The calculation confirms that this point moves in accordance with Eq. (21) where $v_0=v_{20}$ and $c_0=c_{20}=\sqrt{\gamma P_{20}V_{20}}$. It can be shown that the second point corresponds to the characteristic $x_{C_0}(t)$ with $x_{C_0}(0)=0$. The direct numerical integration of Eq. (16) gives the result shown by the dotted curve in Fig. 1. One can see that on the x-ρ plane the C_0 characteristic indeed goes through the kink positions following from Eqs. (9)–(11).

Profiles of pressure calculated for the same initial conditions are shown in Fig. 2. One can see that the pressure jump at the shock front, P_2-P_1, becomes larger at later stages of irradiation. We have checked that the density and pressure jumps at $x=x_{\rm sh}$ satisfy the Hugoniot adiabate given by Eq. (25). In accordance with Eq. (19), pressure increases linearly with t at $x\to\pm\infty$. At known ρ and P the sound velocity c_s can be calculated by using the first equality in Eq. (20). In the case of the ideal gas c_s is proportional to $\sqrt{T}$. The results of the calculation are shown in Fig. 3. It is seen that the jump in c_s, and therefore also in T, practically does not increase with t. At large t the asymptotic values of c_s at $x\to\pm\infty$ become nearly equal. This agrees with Eq. (20). Indeed, at $t\gg c_{20}^2/\lambda$ one obtains the relations

$$\lim_{x\to\pm\infty} c_s \simeq \frac{3}{2}\xi_0\sqrt{\lambda t}, \tag{29}$$

where ξ_0 is defined by Eq. (24).

Figure 4 shows the results for the flow velocity profiles. Similar to density, values of v do not change with t at $x\to\pm\infty$. However, the flow velocities in the perturbed region diminish as compared to initial values. As will be shown in the next section these velocities become negative at late stages of irradiation. Numerical values of the velocity jump agree with conditions given in Eq. (25) (see Ref. [7]). At large t this jump increases approximately proportional to $\sqrt{t}$.

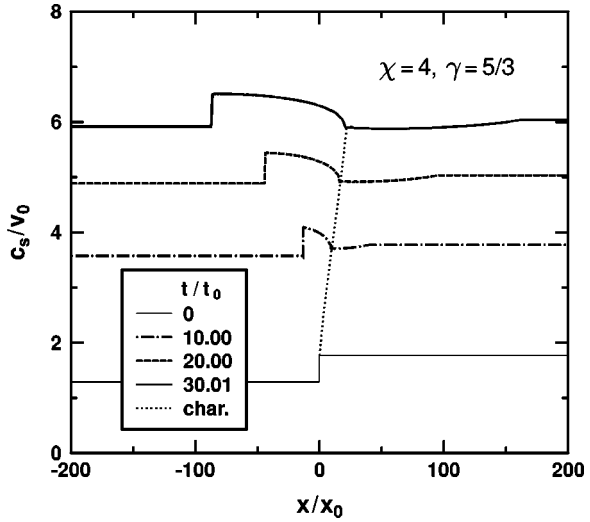

FIG. 3. The same as in Fig. 1, but for sound velocity profiles.

B. Self-similarity of flow at large irradiation time

The results presented in Sec. III A suggest that at large irradiation time, the fluid dynamical quantities exhibit some properties of self-similarity. At $t\gg c_{20}^2/\lambda$ characteristic values of pressure and sound velocity increase, respectively, proportional to t and $\sqrt{t}$. On the other hand, at late stages of irradiation the size of the region with a perturbed flow grows approximately proportional to $t^{3/2}$. This means that at $t\to\infty$ the following relations should hold asymptotically

$$V\simeq V_{\rm as}=\rho_0^{-1}\hat{V}(\xi), \tag{30}$$

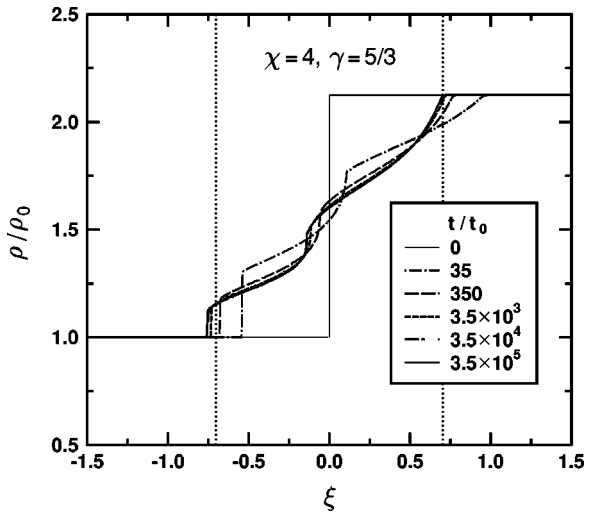

FIG. 5. The density profiles at large irradiation times as functions of $\xi = x(\lambda t^3)^{-1/2}$. The dotted vertical lines show positions of the $C_{\pm}$ characteristics (23).

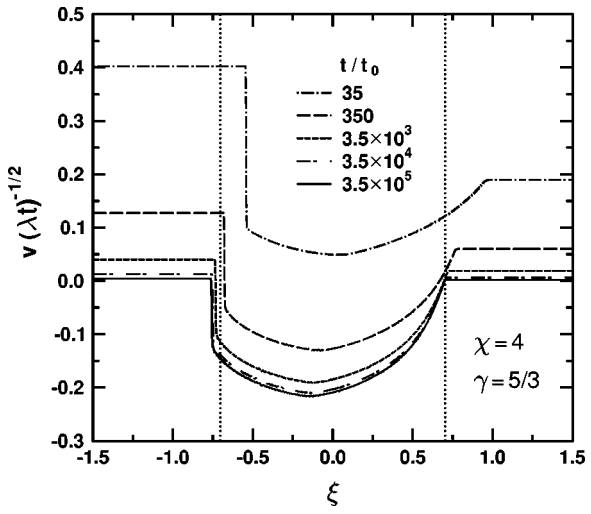

FIG. 6. The same as in Fig. 5, but for the scaled velocity profiles.

$$v \simeq v_{\rm as} = \sqrt{\lambda t}\hat{v}(\xi), \tag{31}$$

$$P \simeq P_{\rm as} = (\gamma - 1)\rho_0 \lambda t \hat{P}(\xi), \tag{32}$$

where scaled dimensionless quantities $\hat{V}, \hat{v}, \hat{P}$ depends on x and t only via the self-similar variable

$$\xi \equiv x/\sqrt{\lambda t^3}. \tag{33}$$

By substituting asymptotic expressions (30)–(32) into the equations of fluid dynamics (9)–(11) one can obtain the set of ordinary differential equations for $\hat{V}$, $\hat{v}$, and $\hat{P}$ (see Appendix). Apparently, these equations cannot be solved analytically. It is possible, however, to find the limiting behavior of flow directly from the numerical solution of Eqs. (9)–(11) at large t.

Figure 5 represents density as function of ξ at several fixed times t. One can see that in agreement with Eq. (30), at large t the density depends on x and t only via ξ. The shock wave does not disappear as $t \to \infty$. At late stages its front accelerates in accordance with the relation

$$x_{\rm sh}(t) \simeq \xi_{\rm sh}\sqrt{\lambda t^3}, \tag{34}$$

where $\xi_{\rm sh}$ is a constant fully determining the asymptotic properties of the shock wave. In particular, $\xi_{\rm sh}$ defines asymptotic behavior of the shock front velocity,

$$D(t) \simeq -\frac{3}{2}\xi_{\rm sh}\sqrt{\lambda t}. \tag{35}$$

As seen in Figs. 5 and 6, the region of the perturbed (nontrivial) flow corresponds to the interval $\xi_{\rm sh} < \xi < \xi_0$. It will be shown below that the asymptotic position of the shock front $\xi = \xi_{\rm sh}$ moves to the left with rising initial pressure ratio χ. For weak initial shocks, $\chi \simeq 1$, the shock front becomes close to the limiting position of the C characteristics, i.e., $\xi_{\rm sh} \simeq -\xi_0$.

Another feature of the self-similar regime, is the appearance of a rapid density variation at some intermediate ξ_* behind the shock front. By analyzing Eqs. (A1)–(A3) (see Appendix) one can show that at large t the disturbed zone is characterized by the combination of a strong discontinuity (the shock front at $\xi = \xi_{\rm sh}$) and two weak discontinuities [9] at $\xi = \xi_*$ and ξ_0. According to Fig. 6 the convergence to the self-similar behavior is much slower for the velocity profiles. It is interesting to note that the flow velocity changes sign at late stages of irradiation. Comparing Figs. 5 and 6, one can see that the point $\xi = \xi_*$ corresponds to the minimum of the asymptotic velocity profile $\hat{v}(\xi)$. This point also gives the limiting position of the C_0 characteristics at $t \to \infty$. Indeed, substituting Eq. (31) into Eq. (16), one can see that all C_0 characteristics satisfy the asymptotic relation $x_{C_0}(t) \simeq \xi_* \sqrt{\lambda t^3}$, where ξ_* is determined from the equation [10]

$$\hat{v}(\xi_*) = \frac{3}{2}\xi_*. \tag{36}$$

Figures 7–9 show asymptotic profiles of flow velocity, density, and pressure calculated for initial ratios $\chi = 2$, 4, and 10. In accordance with the above discussion, the line $3\xi/2$ goes through minima of the asymptotic velocity profiles at different χ. This is clearly seen in Fig. 7. Asymptotic density profiles are shown in Fig. 8. Here the points ξ_* are marked by arrows. Figure 9 shows the asymptotic pressure profiles that, unlike the density profiles, vary smoothly at $\xi = \xi_*$.

Jumps of asymptotic parameters at the shock front $\xi = \xi_{\rm sh}$ can be determined by using Eqs. (25) in the limit $t \to \infty$. At $\xi < \xi_{\rm sh}$ one has $\hat{v} = 0$ and $\hat{P} = \hat{V} = 1$. Marking the flow parameters at $\xi = \xi_{\rm sh} + 0$ by indices "sh," one gets the relations

$$-\frac{3}{2}\xi_{\rm sh} = \frac{\hat{v}_{\rm sh} - \frac{3}{2}\xi_{\rm sh}}{\hat{V}_{\rm sh}} = \sqrt{(\gamma - 1)\frac{\hat{P}_{\rm sh} - 1}{1 - \hat{V}_{\rm sh}}} = \frac{3}{2}\xi_0\sqrt{\frac{1 + \hat{P}_{\rm sh}}{1 + \hat{V}_{\rm sh}}}. \tag{37}$$

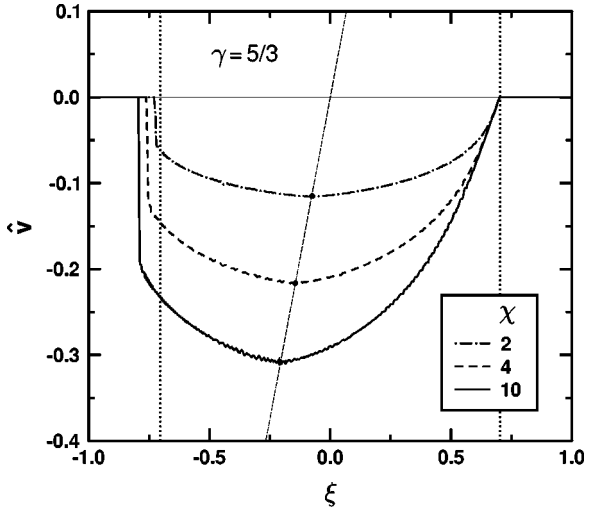

FIG. 7. Asymptotic profiles of scaled velocity at various ratios of initial pressure χ. The thin dashed curve corresponds to the line $3\xi/2$. The dots indicate points of minimal velocities. Dotted lines are the same as in Fig. 5.

Using these conditions, $\hat{v}_{\rm sh}$, $\hat{P}_{\rm sh}$, and $\hat{V}_{\rm sh}$ may be obtained as functions of $\xi_{\rm sh}$. For example, the scaled pressure behind the shock front is equal to

$$\hat{P}_{\rm sh}=1+\frac{2\gamma}{\gamma+1}\left(\frac{\xi_{\rm sh}^2}{\xi_0^2}-1\right). \tag{38}$$

Substituting in Eq. (37) the values of $\xi_{\rm sh}$ determined from numerical solution of fluid-dynamical equations, one may calculate asymptotic parameters of the shock wave at given χ. The results of this calculation are shown in Table I. It has been checked that these results agree well with jumps of flow velocity, density, and pressure in Figs. 7–9. The last column gives the points where asymptotic velocities achieve their minima.

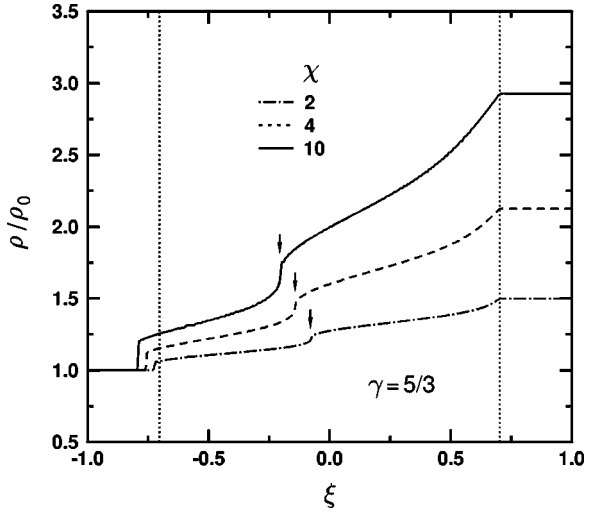

FIG. 8. Asymptotic density profiles at various χ. The arrows indicate the values of ξ_*, defined by Eq. (36). The dotted lines are the same as in Fig. 5.

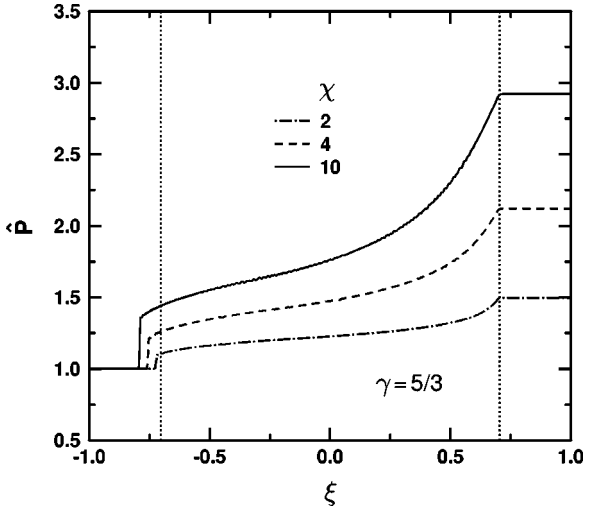

FIG. 9. Asymptotic profiles of pressure at various χ. The dotted lines are the same as in Fig. 5.

IV. SIMULATION OF IRRADIATED SHOCKS UNDER LABORATORY CONDITIONS

Experimental investigation of the effects studied in this paper will be possible in the laboratory by depositing energy into a target with a long deposition length. The only practical means for doing this is the use of heavy-ion beams. We have, therefore, performed realistic hydrodynamic simulations to estimate the magnitude of the effect with heavy-ion beams such as will be available with the proposed enhanced accelerator [11] at the GSI laboratory, Germany. In all calculations presented in this section we consider cylindrical targets made of solid gold. The targets were irradiated by singly ionized uranium beams collinear with target axes. In all cases the bombarding energy of heavy ions was 500 MeV per nucleon.

The simulations were performed using the code CAVEAT developed at Los Alamos [12]. The code solves the fluid-dynamical equations using the *Arbitrary Lagrangian-Eulerian* (ALE) technique and the second-order Godunov-type scheme. Local values of ion energy deposition were calculated by decomposing the beam into a large number of beamlets and tracing them through the moving cells. Effects of thermal conductivity and viscosity were neglected.

In the first simulation the target had 3 mm radius and 6 mm length. It was assumed that the beam had constant radial and temporal profiles with the beam radius $r_b=2$ mm and the pulse duration $\tau=50$ ns. The total penetration range of a 500 MeV/A uranium ion in solid gold of normal density is about 3.5 mm. The total deposited energy of the beam was

TABLE I. Parameters of asymptotic flow behind the shock wave ($\gamma=5/3$).

χ	$\xi_{\rm sh}$	$\hat{V}_{\rm sh}^{-1}$	$\hat{v}_{\rm sh}$	$\hat{P}_{\rm sh}$	ξ_*
2	−0.720	1.038	−0.040	1.062	−0.074
4	−0.759	1.120	−0.122	1.208	−0.144
10	−0.785	1.176	−0.175	1.310	−0.209

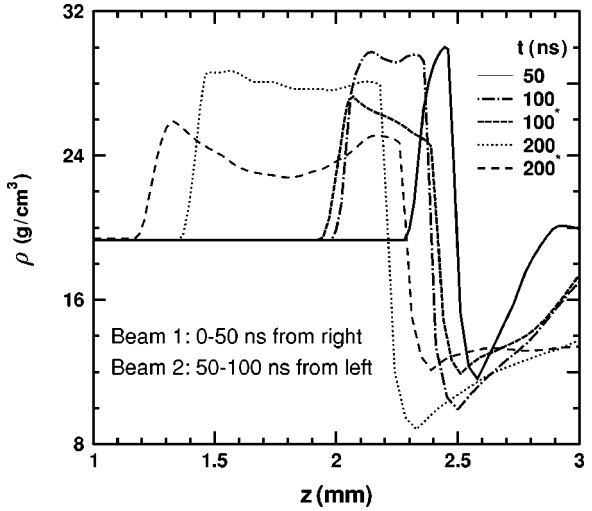

FIG. 10. Profiles of density along the axis of a cylindrical solid gold target irradiated by a heavy-ion beam of 50 ns duration from the right at various times (the parameters of the beam are given in the text). The curves for times marked with an asterisk correspond to the situation with an additional beam of the same properties impinging on the target from the left after the first beam has ended.

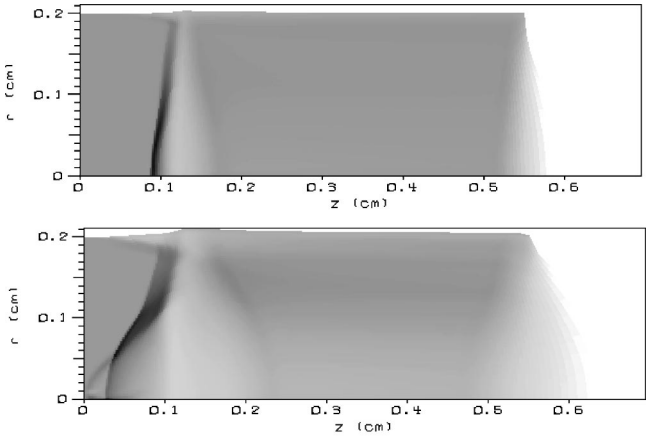

FIG. 11. Density plots of a gold cylinder irradiated by a heavy-ion beam from the right. The darkness of shading is proportional to the density of matter. Upper and lower plots correspond to irradiation times 6 and 12 ns, respectively. The curved shock front is clearly developed after 6 ns, but is destroyed in the center already at 12 ns. The effects of beam penetration through the shock front are also visible at this time. Note that the gray scale is different in two plots, it was chosen to show geometrical effects more clearly.

38.1 kJ. In the considered case the specific deposition rate $\lambda(x)$ can be evaluated as

$$\lambda(x)=\frac{N}{\pi r_b^2 \tau}\frac{dE}{\rho\, dx}. \tag{39}$$

Here dE/dx is the energy loss per unit path length of a single ion in a target material of the density ρ, N is the total number of bombarding ions. The ion deposition profiles dE/dx have been calculated by using a realistic deposition model realized in the TRIM code [13]. The equation of state for gold was taken from the SESAME [14] tables. In fact, we solved the fluid-dynamical equations analogous to Eqs. (3)–(5), but generalized for the case of two-dimensional (axially symmetric) cylindrical flow.

Two situations were compared in our simulations. First, we consider irradiation with one beam from the right, and the same with a second beam of identical properties from the left starting with a 50 ns delay, i.e., exactly after the end of the first beam. The target length is chosen such that the second beam completely penetrates the running shock wave, and although the realistic deposition profile is used, the second Bragg peak is sufficiently far to the right of the shock. As a consequence, the local deposition from the second beam is approximately constant inside the shock. Figure 10 compares density profiles along the target axis ($r=0$) for the two cases at several times between 50 and 200 ns. At $t=50$ ns the density profile is, of course, not yet disturbed by the second beam. One can clearly see that the shock without irradiation runs towards the left, losing speed and amplitude rather slowly at t between 50 and 200 ns. A weaker shock caused by the backward side of the Bragg peak is not visible since its position is to the right of the region plotted in Fig. 10. The decay in the shock strength due to the additional deposition of energy is clearly visible already at $t=100$ ns. The shock moves faster and the density of matter behind its front diminishes in accordance with the predictions of the simplified model studied in Sec. III. At $t=200$ ns the density jump is reduced by about 30–50 %. The shock speed has increased by about 20%, which should be clearly observable in experiments. The additional structure in the compressed region is apparently caused by the nonuniform deposition of the beam.

Another possible scenario may exist even for a single beam irradiation. In the case when the beam has long enough duration, the sideward expansion of the target material will result in depletion of density and, therefore, in a longer range of bombarding particles near the target axis. This enhanced range can lead to beam penetrating through the shock wave created at the initial stages of target irradiation. As a consequence, at late stages the shock wave will be weaker in a central region of the target. An example of such configuration is shown in Fig. 11. In this case the target had a radius of 2 mm and a length of 5 mm. The beam had the same properties as above, except that its radial profile was assumed to be Gaussian with a full width at half maximum of 1.5 mm. The Gaussian profile was chosen not only because it is more realistic, but also because in this case the density starts decreasing immediately after beginning of irradiation even near the axis of the target. The results of calculation demonstrate how the original curved shock front created by the beam is destroyed in the center, leading to a ringlike structure. This effect can be observed after the shock wave emerges from the other end of the target.

To check whether the effect might be observable with heavy-ion beams that will be available at the first stage [11] of the upgraded GSI facility we have performed two additional calculations for smaller beam intensities. In the first calculation both beams (the first one generating the shock and the second beam irradiating it) had equal total energies,

reduced by factor 5 as compared to previous cases. We chose the beam duration $\tau=300$ ns and radius $r_b=5$ mm. The target had 3 mm radius and 6 mm length. In the second calculation the beam generating the shock wave was replaced by a stronger beam with parameters considered in the first series of simulations (see Fig. 10 and Ref. [5]). In both calculations the modifications of shock velocities and compression ratios turned out to be at the percentage scale that is below the measurable level. Therefore, experimental investigation of the effects predicted in this paper requires intensive heavy-ion beams that will be available only at the fully upgraded GSI facility.

V. SUMMARY AND OUTLOOK

In this paper we have investigated the behavior of a shock wave stimulated by energy deposition. The case of a planar shock wave under the influence of homogeneous irradiation has been studied in detail. This was done by solving the one-dimensional fluid-dynamical equations. It is shown that the initial shock discontinuity decays into accelerated shock wave and a simple wave propagating into the postshock matter. It is found that the flow exhibits a self-similar behavior at late times.

The fluid-dynamical simulations have also been performed for the more realistic conditions expected for laboratory experiments. We have studied the behavior of a shock wave under the influence of additional energy deposition produced by a heavy-ion beam in a cylindrical target and found that the main features of the above planar solution are also reproduced in this more realistic situation. Another interesting effect studied is the weakening of the shock wave in the vicinity of the target axis due to the sideward expansion of matter and the increased deposition length of bombarding ions. These examples represent possible experimental setups for studying the effects of energy deposition on the structure of shock waves. Such experiments are possible at any laboratory having intensive heavy-ion beams with high enough deposition energies.

In the future we are planning to study analogous processes in the case of spherical geometry and nonuniform density distributions that is more relevant for supernovae explosions. A more quantitative study of stimulated shock dynamics should include effects of internal heat transport and viscosity. It is interesting also to investigate the role played by endothermic and exothermic reactions during the propagation of a shock front.

ACKNOWLEDGMENTS

This work has been supported by the RFBR Grant No. 00–15–96590, GSI, BMBF, and WTZ.

APPENDIX: EQUATIONS FOR ASYMPTOTIC FLOW PROFILES

Inserting expressions (30)–(32) into Eqs. (9)–(11) one obtains the coupled set of ordinary differential equations for asymptotic profiles $\hat{V}(\xi)$, $\hat{v}(\xi)$, and $\hat{P}(\xi)$

$$\left(\hat{v}-\frac{3}{2}\xi\right)\hat{V}'=\hat{v}'\hat{V}, \tag{A1}$$

$$\left(\hat{v}-\frac{3}{2}\xi\right)\hat{v}'+(\gamma-1)\hat{P}'\hat{V}=-\frac{\hat{v}}{2}, \tag{A2}$$

$$\left(\hat{v}-\frac{3}{2}\xi\right)\hat{P}'+(\gamma\hat{v}'+1)\hat{P}=\frac{1}{\hat{V}}, \tag{A3}$$

where primes denote derivatives with respect to ξ. The boundary conditions for these equations may be derived from Eqs. (17)–(19). At $t\to\infty$, using Eqs. (30)–(32) one has

$$\hat{v}(\pm\infty)=0, \tag{A4}$$

$$\hat{P}(-\infty)=\hat{V}(-\infty)=1, \tag{A5}$$

$$\hat{P}(+\infty)=\hat{V}^{-1}(+\infty)=\rho_{20}/\rho_0. \tag{A6}$$

The above equations are trivially satisfied in the regions $\xi>\xi_0$ and $\xi<\xi_{\rm sh}$. Therefore, it is sufficient to solve Eqs. (A1)–(A3) only in the interval $(\xi_{\rm sh},\xi_0)$. The boundary conditions at $\xi=\xi_0$ are given by Eqs. (A4) and (A6) with the replacement $+\infty\to\xi_0$. The parameters of asymptotic flow at $\xi=\xi_{\rm sh}+0$ can be determined from Eq. (37). They are functions of the shock wave position $\xi_{\rm sh}$.

One can rewrite Eqs. (A1)–(A3) in the vector form

$$A\hat{\boldsymbol{y}}'=\boldsymbol{B}, \tag{A7}$$

where $\hat{\boldsymbol{y}}$ is a column with the components $\hat{V},\hat{v},\hat{P}$. The matrix A and the vector $\boldsymbol{B}$ may be easily obtained from the above set of equations. The derivatives $\hat{\boldsymbol{y}}'$ and the matrix A^{-1} do not exist at the points ξ where

$$\det A=\left(\hat{v}-\frac{3}{2}\xi\right)\left[\left(\hat{v}-\frac{3}{2}\xi\right)^2-\hat{c}^2\right]=0. \tag{A8}$$

Here $\hat{c}=\frac{3}{2}\xi_0\sqrt{\hat{P}\hat{V}}$ is the scaled sound velocity. Comparing this equation with Eqs. (14)–(16) one can see that solutions of Eq. (A8) give the asymptotic positions of the $C_\pm$ and C_0 characteristics. The latter is defined by Eq. (36).

In fact, the right boundary of the nontrivial region, $\xi=\xi_0$, is the C_+ characteristic. At this point $\hat{v}'$ jumps from zero (at $\xi>\xi_0$) to some finite value $a_v\equiv\hat{v}'(\xi_0-0)$. By using Eqs. (A1)–(A3) for small $\xi_0-\xi$, one can show that their solution between the characteristics C_+ and C_0, i.e., in the interval (ξ_*,ξ_0), is a functional of the parameters a_v and ρ_{20}/ρ_0. At given a_v one can solve Eqs. (A1)–(A3) in the whole interval. Below this solution is marked by the subscript "+."

On the other hand, choosing some value of $\xi_{\rm sh}$ and calculating $\hat{\boldsymbol{y}}(\xi_{\rm sh}+0)$, one can find the solution of Eqs. (A1)–(A3) between the shock front and the C_0 characteristic, i.e., in the

interval (ξ_{sh},ξ_*). The corresponding solution (denoted below by the subscript "$-$") is fully determined by the parameter ξ_{sh}. Matching the solutions $\hat{\boldsymbol{y}}_+$ and $\hat{\boldsymbol{y}}_-$ at $\xi=\xi_*$ gives three conditions for determining three unknown parameters ξ_{sh}, ξ_*, and a_v,

$$\hat{v}_-(\xi_*)=\hat{v}_+(\xi_*)=\frac{3}{2}\xi_*, \tag{A9}$$

$$\hat{P}_-(\xi_*)=\hat{P}_+(\xi_*). \tag{A10}$$

By using Eqs. (A9) and (A10) and Eqs. (A1)–(A3) it may be shown that $\hat{V}$ will be also continuous at $\xi=\xi_*$.

A "shooting" method may then be used to find ξ_{sh} and asymptotic flow profiles $\hat{\boldsymbol{y}}(\xi)$ at different pressure ratios χ. These calculations agree well with the results obtained in Sec. III B.

[1] B. Leibundgut, Astron. Astrophys. Rev. **10**, 179 (2001).

[2] H.A. Bethe and J.R. Wilson, Astrophys. J. **295**, 14 (1985).

[3] H.-Th. Janka, e-print astro-ph/0008432.

[4] L.D. Landau and E.M. Lifshitz, *Fluid Mechanics* (Pergamon, New York, 1987).

[5] It is, of course, irrelevant how the shock itself is created—instead of a heavy-ion beam a laser could be used, for example, and the second beam could come from any suitable direction.

[6] J.A. Maruhn, K.-J. Lutz, F. Illenberger, and S. Bernard, Nucl. Instrum. Methods Phys. Res. A **415**, 98 (1998); N.A. Tahir, D.H.H. Hoffmann, J.A. Maruhn, K.-J. Lutz, and R. Bock, Phys. Plasmas **5**, 4426 (1998).

[7] It is worth noting that the last equality in Eq. (25) is in fact the Rankine-Hugoniot relation. Excluding D from the first two relations one can find that the velocity jump is equal to $v_1-v_2=\sqrt{(P_2-P_1)(V_1-V_2)}$.

[8] J.P. Boris and D.L. Book, J. Comput. Phys. **11**, 38 (1973); D.L. Book, J.P. Boris, and K. Hain, *ibid.* **18**, 248 (1975).

[9] In such discontinuities spatial derivatives of fluid-dynamical variables are infinite or exhibit jumps.

[10] According to Eq. (A1), $\hat{v}$ is minimal at $\xi=\xi_*$.

[11] For the ongoing discussion about this project see http://www.gsi.de/GSI-Future/

[12] F.L. Addessio *et al.*, LANL Report No. LA-10613-MS, 1992 (unpublished).

[13] J.F. Ziegler and J.P. Biersack, *The Stopping and Range of Ions in Solids* (Pergamon, New York, 1985).

[14] LANL Report No. LA-UR-92-3407, edited by S.P. Lyon and J.D. Johnson, 1992 (unpublished).